INTERFACE

royalsocietypublishing.org/journal/rsif

Research

Check for updates

Cite this article: Murtada S-I *et al*. 2020 Paradoxical aortic stiffening and subsequent cardiac dysfunction in Hutchinson–Gilford progeria syndrome. *J. R. Soc. Interface* **17**: 20200066.
http://dx.doi.org/10.1098/rsif.2020.0066

Received: 30 January 2020
Accepted: 30 April 2020

Subject Category:
Life Sciences–Engineering interface

Subject Areas:
biomechanics, biomedical engineering

Keywords:
progeria, aortic stiffness, pulse wave velocity, diastolic dysfunction, allometric scaling, ageing

Authors for correspondence:
S.-I. Murtada
e-mail: sae-il.murtada@yale.edu
J. D. Humphrey
e-mail: jay.humphrey@yale.edu

Electronic supplementary material is available online at https://doi.org/10.6084/m9.figshare.c.4977704.

THE ROYAL SOCIETY PUBLISHING

Paradoxical aortic stiffening and subsequent cardiac dysfunction in Hutchinson–Gilford progeria syndrome

S.-I. Murtada[1], Y. Kawamura[1], A. W. Caulk[1], H. Ahmadzadeh[1], N. Mikush[2], K. Zimmerman[3], D. Kavanagh[3], D. Weiss[1], M. Latorre[1], Z. W. Zhuang[4], G. S. Shadel[6], D. T. Braddock[3] and J. D. Humphrey[1,5]

[1]Department of Biomedical Engineering, Yale University, New Haven, CT, USA
[2]Translational Research Imaging Center, [3]Department of Pathology, [4]Section of Cardiovascular Medicine, and [5]Vascular Biology and Therapeutics Program, Yale School of Medicine, New Haven, CT, USA
[6]Molecular and Cellular Biology, Salk Institute for Biological Studies, La Jolla, CA, USA

S-IM, 0000-0002-6578-4585; YK, 0000-0003-2137-6464; HA, 0000-0002-2424-1867; JDH, 0000-0003-1011-2025

Hutchinson–Gilford progeria syndrome (HGPS) is an ultra-rare disorder with devastating sequelae resulting in early death, presently thought to stem primarily from cardiovascular events. We analyse novel longitudinal cardiovascular data from a mouse model of HGPS (*Lmna*$^{G609G/G609G}$) using allometric scaling, biomechanical phenotyping, and advanced computational modelling and show that late-stage diastolic dysfunction, with preserved systolic function, emerges with an increase in the pulse wave velocity and an associated loss of aortic function, independent of sex. Specifically, there is a dramatic late-stage loss of smooth muscle function and cells and an excessive accumulation of proteoglycans along the aorta, which result in a loss of biomechanical function (contractility and elastic energy storage) and a marked structural stiffening despite a distinctly low intrinsic material stiffness that is consistent with the lack of functional lamin A. Importantly, the vascular function appears to arise normally from the low-stress environment of development, only to succumb progressively to pressure-related effects of the lamin A mutation and become extreme in the peri-morbid period. Because the dramatic life-threatening aortic phenotype manifests during the last third of life there may be a therapeutic window in maturity that could alleviate concerns with therapies administered during early periods of arterial development.

1. Introduction

Hutchinson–Gilford progeria syndrome (HGPS) is a genetic disorder characterized by premature ageing with devastating consequences to cardiovascular and musculoskeletal tissues. Accelerated atherosclerosis, which can lead to myocardial infarction or stroke, was thought to cause death in the early teens [1] but statins and lipid-lowering agents did not improve lifespan. HGPS also accelerates the structural stiffening of central arteries, as inferred from pulse wave velocity (PWV) [2]. Increased central artery stiffness is an initiator and indicator of diverse cardiovascular diseases in the general population and thus a predictor of all-cause mortality [3], particularly due to myocardial infarction, stroke and heart failure [4]. Importantly, a recent study revealed that left ventricular diastolic dysfunction was the most prevalent abnormality in patients having HGPS [5], and a recent clinical trial identified heart failure as the primary cause of death [6]. There is, therefore, a pressing need to investigate together the changes in central vessels and cardiac function. Given the scarcity of human data, mouse models enable more detailed study of both the underlying mechanisms and resulting clinical phenotypes.

HGPS arises from point mutations in the gene (*LMNA*) that encodes the cell nuclear envelope protein lamin A [7,8], which normally contributes to nuclear stiffness and transcriptional regulation [9] and is highly mechanosensitive [10]. Mutations can lead to an altered lamin A precursor, resulting in a truncated form of lamin A called progerin (from the Greek, *pro* [before] *geras* [old age]). Using a bacterial artificial chromosome approach, a transgenic mouse model was generated having the human mutation (c.1824C>T;pG608G). Central arteries from these mice exhibit fewer smooth muscle cells (SMCs), medial calcification, accumulated proteoglycans, disorganized collagen and some fragmented elastic fibres [11]. Such changes in composition and microstructure would be expected to compromise the biomechanical functionality of the arterial wall. Indeed, it was suggested that arterial SMCs in this mouse 'are especially vulnerable to the mechanical stress imposed on them' despite blood pressure remaining nearly normal [12]. Surprisingly, detailed quantification of arterial function and properties remains wanting, though a recent study reported stiffening of the thoracic aorta and mesenteric artery in another mouse model of HGPS [13], generated using a knock-in mutant allele that carries a c.1827C>T; p.G609G mutation [14], denoted $Lmna^{G609G/G609G}$. The associated cardiovascular phenotype has yet to be examined in detail, including longitudinally, but there is the loss of SMCs and calcification of the aortic media in $Lmna^{G609G/+}$ mice [15] and decreased SMCs, decreased elastic fibre waviness, and increased collagen in $Lmna^{G609G/G609G}$ mice [13].

Normal ageing progressively and differentially affects the aorta along its length [16,17], hence effects of HGPS should be quantified as a function of age and aortic location. Our aim was to biomechanically phenotype the thoracic and abdominal aorta in adult male and female $Lmna^{G609G/G609G}$ mice and to evaluate associated effects on the heart. We thus quantified cardiac function and central haemodynamics *in vivo* as well as SMC contractility and biaxial passive aortic properties *ex vivo*; we also used a novel computational model to associate changes in biomechanical behaviour with observed microstructural features. The implications of these findings are interpreted, in part, via direct comparisons to similar data for mice that have aged normally, have germline mutations that compromise elastic fibre integrity, a feature common in central artery ageing, or have induced hypertension, which also arises in ageing.

2. Methods

2.1. Animals

All animal protocols were approved by the Institutional Animal Care and Use Committee of Yale University. Mice were generated using heterozygous ($Lmna^{G609G/+}$) breeding pairs. A total of 37 female (F) and male (M) control ($Lmna^{+/+}$ or simply *Wt*) and progeria ($Lmna^{G609G/G609G}$ or simply *G609G*) offspring were studied at either 100 days (d) of age (approx. 14 weeks) or 140 d of age (20 weeks), the latter to study the peri-morbid condition since these progeria mice died around 150 d of age. As we reported at the 20–24 September 2018 Progeria Research Foundation meeting, this extension in lifespan beyond the expected 103 d [13] was achieved by providing moist chow on the floor of the cages to facilitate eating as the mice became progressively weaker. We did not use a high-fat diet to extend lifespan further, however [18], to avoid possible atherosclerotic complications. Conscious blood pressures were measured using a standard tail-cuff device (Kent Scientific). At the appropriate endpoint, at times following the collection of *in vivo* data, an intraperitoneal injection of Beuthanasia-D was used to euthanize the mice and the aorta was excised from its root to the aortic bifurcation. These excised vessels were used for *ex vivo* biomechanical evaluation and subsequent (immuno)histological examination as described below.

2.2. Ultrasound and micro-CT

Echocardiographic and vascular ultrasonic data were collected *in vivo*, under isoflurane anaesthesia, on a sub-group of 140-day-old female wild-type littermate ($n = 3$) and progeria ($n = 5$) mice, followed by micro-CT imaging. These data were contrasted with data on approximately 140-day-old non-littermate wild-type female mice ($n = 3$–6). Non-invasive echocardiographic and vascular ultrasonic data were collected using a Visualsonic Vevo 2100 system with a linear array probe (22–55 MHz). Systolic and diastolic function of the left ventricle (LV) was quantified using standard methods [19]. Briefly, B-Mode imaging in parasternal long axis (LAX) and short axis (SAX) views and M-Mode imaging in both planes tracked cavity diameter at the level of the papillary muscles to measure LV systolic function. B-Mode images of the LV outflow tract diameter and pulsed-wave Doppler images of blood velocity patterns across the aortic valve estimated aortic valve area to check for valve stenosis; no aortic regurgitation was noted. LV diastolic function was monitored using an apical four-chamber view, which was achieved by aligning the ultrasound beam with the cardiac LAX. Colour Doppler imaging located the mitral valve, while pulsed-wave Doppler measured mitral inflow velocity. Finally, Doppler tissue imaging from the lateral wall and interventricular septum measured velocities associated with tissue motion. PW Doppler measured near centreline blood velocities proximally (near the aortic root) and distally (close to the aortic bifurcation), which enabled assessment of pulse wave transit times.

The aortic path length travelled by the pulse wave (from the ascending aorta to the aortic bifurcation) was measured *in vivo* from micro-CT angiograms ($n = 6$ controls, of which three were littermate controls, and $n = 5$ progeria mice). Briefly, following a bolus intrajugular injection of 5 ml kg^{-1} exia 160 contrast agent (Binitio Biomedical Inc.), mice were imaged in a micro-CT scanner (MILabs) at 50 kV tube voltage, 0.48 mA tube current, 40 ms exposure and 480 projections. Projections from each scan were reconstructed into three-dimensional volumes, with a voxel size of $80 \times 80 \times 80\ \mu m^3$. Arterial cross-sections along the aortic tree were segmented semi-automatically using a two-dimensional level-set method using the open source software package *CRIMSON* (www.Crimson.org).

2.3. Allometric scaling

Given the markedly reduced body mass of the progeria mice at all ages beyond postnatal day approximately 42, independent of sex, we considered possible allometric scaling of the form $y = cM^k$, where y is any dimensional metric of interest (e.g. cardiac output or luminal diameter), M is the body mass (in grams) and c and k are the allometric constants determined from linear regression of data from normal wild-type mice [19] plotted as $\ln(y) = \ln(c) + k\ln(M)$, with ln the natural logarithm. Data from the progeria mice were then plotted along with the allometric data from sex-matched wild-type control mice to determine congruency or not with normal scaling.

2.4. Biomechanical testing

We studied proximal and distal aortic regions: descending thoracic aorta (DTA) and infrarenal abdominal aorta (IAA). To facilitate direct comparison of the present data ($n = 5$ M and 5 F *Wt* and $n = 5$ M and 5 F *G609G* aortas at 140 d and $n = 4$ mixed-sex *Wt*

and $n = 5$ mixed-sex *G609G* aortas at 100 d, noting that there were no sex differences in the extreme, late-stage period and thus we pooled data at 100 d) with previously reported data for multiple mouse models, we used the same validated methods of biaxial testing and data analysis, including constitutive modelling [20]. Briefly, segments from each aortic region were isolated by blunt dissection, cannulated and placed within our custom computer-controlled testing device within a Krebs–Ringer's solution at 37°C (for active studies) or a Hank's buffered solution at room temperature (for passive studies). For the active tests, vessels were set at their *in vivo* length (estimated *ex vivo* under passive conditions as the aortic length at which the transducer-measured axial force did not change upon cyclic pressurization) and pressurized at 90 mmHg [21]. The vessels were then contracted sequentially with two vasoactive stimuli: 100 mM potassium chloride (KCl), which depolarizes the cell membrane and increases intracellular calcium, and 1 µM phenylephrine (PE), which is an alpha-adrenergic agonist. For the subsequent passive tests, vessels were exposed to Hank's solution, then preconditioned via cyclic pressurization from approximately 10 to 140 mmHg while held at their individual *in vivo* axial length and subjected to a series of seven biaxial protocols: cyclic pressurization from approximately 10 to 140 mmHg at three values of axial stretch (95, 100 and 105% of the *in vivo* value) and cyclic axial stretching at four fixed values of luminal pressure (10, 60, 100 or 140 mmHg). Having data slightly above and below the *in vivo* state facilitates robust parameter estimation for the constitutive model [17,20]. Data collected online included outer diameter, luminal pressure, axial length and axial force.

We conclude by noting that biaxial tests, both active and passive, are critical for evaluating arterial behaviour under physiologically meaningful conditions. The only prior passive biomechanical tests reported on vessels from progeria mice were based on wire or pressure myography [15], neither of which captures the full biomechanical behaviour and thus are insufficient for detailed phenotyping.

2.5. Biomechanical properties

Data from the unloading portions of the last cycles of the seven passive pressure–diameter and axial force–length protocols were fit simultaneously using a Levenberg–Marquardt nonlinear regression and a validated nonlinear stored energy function W [20,22]. This function accounts for isotropic contributions of an amorphous matrix (via a neo-Hookean function, which has proven reliable in many prior studies), thought to arise mainly from elastin and glycosaminoglycans (GAGs), and anisotropic contributions due to multiple families of locally parallel collagen fibres (with copious unquantified cross-links and physical entanglements captured phenomenologically by four families) and circumferentially oriented passive smooth muscle (via Fung-type exponential functions), namely

$$W(\mathbf{C}, \mathbf{M}^i) = \frac{c}{2}(I_\mathbf{C} - 3) + \sum_{i=1}^{4} \frac{c_1^i}{4c_2^i}\{\exp[c_2^i(IV_\mathbf{C}^i - 1)^2] - 1\}, \quad (2.1)$$

where $I_\mathbf{C} = tr(\mathbf{C})$ and $IV_\mathbf{C}^i = \mathbf{C} : \mathbf{M}^i \otimes \mathbf{M}^i$, with $\mathbf{C} = \mathbf{F}^\mathrm{T}\mathbf{F}$ computed from the deformation gradient tensor $\mathbf{F} = \mathrm{diag}[\lambda_r, \lambda_\theta, \lambda_z]$ that is inferred directly from experimental measurements of changes in diameter and length, which define the stretch ratios λ_i, with $\det(\mathbf{F}) = 1$ because of assumed incompressibility of the wall. The direction of the ith family of fibres in the traction-free reference configuration is $\mathbf{M}^i = [0,\ \sin\alpha_0^i,\ \cos\alpha_0^i]$, with angle α_0^i defined relative to the axial direction. Based on prior microstructural observations for wild-type elastic arteries, and the yet unquantified effects of copious cross-links among the multiple families of fibres, we include possible axial ($\alpha_0^1 = 0$), circumferential ($\alpha_0^2 = \pi/2$) and two symmetric diagonal families of fibres ($\alpha_0^{3,4} = \pm\alpha_0$). Hence, the eight model parameters are: c, c_1^1, c_2^1, c_1^2, c_2^2, $c_1^{3,4}$, $c_2^{3,4}$ and α_0. Values of biaxial stress and material stiffness are computed from appropriate differentiation of the stored energy function, then compared at physiologic pressures and individual *in vivo* values of axial stretch.

2.6. Histology and immunohistochemistry

Following *ex vivo* testing, samples were fixed overnight in 10% formalin while unloaded, then stored in 70% ethanol at 4°C until embedding in paraffin and sectioning at 5 µm. Sections were stained with haematoxylin and eosin (H&E) to count cell nuclei, Verhoff Van Gieson (VVG) to quantify elastic fibres (black), Movat's pentachrome (MOV) to quantify intramural proteoglycans (blue), Masson's trichrome to quantify cytoplasm (red) and fibrillar collagen (blue), and picro-sirius red (PSR) to delineate collagen fibre size under polarized light (red to green). Slides were imaged using an Olympus BX/51 microscope, with bright- and dark-field imaging at 20× magnification. We analysed three cross-sections for each sample and stain to reduce intra-specimen variability. We used previously developed custom MATLAB software to identify absolute values and area fractions of each load-bearing constituent [23]. Briefly, background subtraction and pixel-based thresholding classified each pixel within the stained sections as elastin, collagen, cytoplasm or medial proteoglycans. Medial and adventitial areas were delineated by the external elastic lamina in MOV images. Immunostaining was used to identify proteoglycans aggrecan and versican. Grey-scaled PSR images were analysed with a curvelet-denoising filter followed by an automated fibre-tracking algorithm combined with CT-FIRE [24] to quantify undulation of collagen fibres; elastin lamellar undulation was determined from VVG-stained sections.

2.7. Particle-based computational model

Whereas the aforementioned continuum model of the arterial wall enables one to compute locally averaged material properties and wall stresses while satisfying mechanical equilibrium, we also used a unique particle-based model to examine individual contributions by the different constituents, and their interactions, including elastic fibres organized into concentric laminae, multiple monolayers of SMCs, collagen fibres and diffuse medial proteoglycans that exhibit Gibbs–Donnan swelling [25]. Briefly, we defined the arterial wall as a collection of $j = 1, 2 \ldots, N$ 'particles' that are endowed with separate biophysical properties and subject to Newton's second law of motion: $\mathbf{f}_j = m_j\ddot{\mathbf{x}}_j$, where m is the mass and $\ddot{\mathbf{x}}$ is the acceleration of particle j. Each particle interacts directly with other particles within a locally defined neighbourhood, defined by a particle list, and continuum-type quantities can be computed by introducing a smoothing (kernel) function

$$\xi(R_k) = \begin{cases} \dfrac{10(h - R_k)^3}{\pi h^5} & R_k \le h \\ 0 & R_k > h \end{cases} \quad (2.2)$$

where $R_k = |\mathbf{X}_k - \mathbf{X}_j|$ denotes the distance between any particle k and particle j, and h defines the 'kernel support'. In this way any quantity of interest g at original particle location $\mathbf{X}_j$ can be computed via

$$\hat{g}(\mathbf{X}_j) = \sum_k g(\mathbf{X}_k) V_k \xi(R_k) \quad (2.3)$$

where V_k denotes the local material volume associated with the listed neighbouring particle k. Further details on the theoretical framework as well as numerical implementation on a high performance computer (Intel Xeon E5-2660 CPU running at 2.6 GHz on 128 cores) can be found elsewhere [25].

Briefly, by mirroring the geometry and microstructural composition of the DTA of the progeria mouse at 100 d of age at the *in vivo* homeostatic state (luminal pressure of 85 mmHg and axial stretch of 1.40), the domain of the model was a portion of cylindrical

wall with inner and outer radii $R_{in} = 434$ µm and $R_{out} = 485$ µm (thus wall thickness $H = 51$ µm), divided into an inner layer representing the media (with thickness $H_M = 39$ µm) and an outer layer representing the adventitia ($H_A = 12$ µm). Because the 100-day-old progeria aorta has minimal proteoglycan accumulation, the wall at this stage was assumed to be devoid of added, swollen proteoglycans. The media was further divided into five alternating layers of elastic laminae, separated by intra-lamellar regions composed of SMCs and collagen. Employing our particle-based framework, this cylindrical domain was discretized into an arrangement of uniformly distributed particles (with inter-particle spacing approx. 2 µm) that represented their surrounding space bounded by their immediate neighbouring particles. The particles positioned at the elastic laminae, intra-lamellar regions and adventitia are colour coded and labelled as elastin (black) particles, intra-lamellar (red or blue) particles and adventitial (green) particles, respectively.

Importantly, the total strain energy function at each particle j having contributions from any normal structural constituent (i.e. elastin, SMCs and collagen) is

$$W(\boldsymbol{C}_j, \boldsymbol{M}_j^k) = \phi_\Gamma^e \left(\frac{\mu}{2}(I_{1j}^e - 3) - \mu \ln J_j + \frac{\hat{\lambda}}{2}(\ln J_j)^2 \right) + \sum_{k=1}^{4} \phi_\Gamma^{c_k} \left(\frac{c_1^k}{4c_2^k}(\exp[c_2^k(I_{4j}^k - 1)^2] - 1) \right). \quad (2.4)$$

The first term represents the isotropic behaviour of elastin networks, which is described by a neo-Hookean material response with shear modulus μ and Lamé constant $\hat{\lambda}$. $I_{1j}^e = \mathrm{tr}(\boldsymbol{C}_j^e) = \mathrm{tr}((\boldsymbol{F}_j^e)^T \boldsymbol{F}_j^e)$ is the first invariant of the right Cauchy–Green tensor ($\boldsymbol{C}_j^e$) where $\boldsymbol{F}_j^e$ is the deformation gradient tensor for elastin (superscript e denotes the elastin). The second term accounts for the directional behaviour of collagen fibres and SMCs. The collagen fibres are again categorized into four directions (or families), denoted by $k = 1$ for axial, $k = 2$ for circumferential and $k = 3,4$ for symmetric diagonal. SMCs are assumed to behave in the circumferential direction, therefore, they are considered as part of a combined contribution with the circumferentially oriented collagen ($k = 2$). Accordingly, c_1^k and c_2^k are the material parameters and $I_{4j}^k = \boldsymbol{C}_j^k : \boldsymbol{M}^k \otimes \boldsymbol{M}^k$ is the square of the stretch in the kth family with $\boldsymbol{M}^k = [0, \sin\alpha, \cos\alpha]$ a unit vector defining the orientation of the fibres ($\alpha = 0,\ 90,\ \pm\alpha_0$ corresponds to axial, circumferential and diagonal directions). In this way, there is considerable consistency between the traditional continuum and particle-based models.

For each group of the particles (elastin, intra-lamellar and adventitial), the total strain energy function has different mixing fractions of elastin and collagen fibres. We multiply the strain energy of each constituent (i.e. elastin and collagen families 'k' denoted by superscripts e and c_k) by an appropriate mass fraction, namely ϕ_Γ^e and $\phi_\Gamma^{c_k}$, where $\Gamma = M_{el}, M_{int}, A$ are used to distinguish elastin, intra-lamellar and adventitial particles, respectively. We use the total deformation gradient ($\boldsymbol{F}_j$) and the corresponding right Cauchy–Green $\boldsymbol{C}_j = (\boldsymbol{F}_j)^T \boldsymbol{F}_j$ tensor to describe deformations from the homeostatic reference to any non-homeostatic configuration. To reproduce the stresses of the wall at the homeostatic reference configuration, we define deposition pre-stretches specific to each constituent in such a way that the resulting wall stress is in equilibrium with the homeostatic pressure and axial stretch. For a particle j, the deposition pre-stretch tensor for elastin is denoted by $\mathbf{G}_{\Gamma j}^e$ and deposition pre-stretches for the SMCs and collagen fibre family k are denoted $\mathrm{G}_{\Gamma j}^k$. By following a prior numerical algorithm [25], the deposition pre-stretches are introduced in the deformation gradient of elastin through $\boldsymbol{F}_j^e = \boldsymbol{F}_j \boldsymbol{G}_{\Gamma j}^e$, and the right Cauchy–Green tensor of collagen by $\boldsymbol{C}_j^k = (G_{\Gamma j}^k)^2 \boldsymbol{C}_j$.

The parameters embedded within the model were estimated using our previous analytical model of a normal aorta and fitting the predicted pressure–outer diameter and axial force–length results to the experimentally measured data for the DTA of the progeria mouse at 100 d of age. Because the analytical approach is based on a bi-layered thin-walled vessel, the obtained parameters are adjusted to account for the lamellar structure of the media in this particle-based model. These parameters are presented in electronic supplementary materials. Finally, to introduce a swelling pressure caused by accumulated proteoglycans in the intra-lamellar regions, we randomly prescribed intra-lamellar particles (i.e. we selected particles stochastically for 10, 20 or 30% GAG content within the media, noting that the different stochastic distributions had no effect on structural stiffness for a given mass fraction of GAGs) and modified their Cauchy stress function to

$$\boldsymbol{\sigma}_j^{GAG} = \frac{1}{J_j}\mu^{GAG}(\boldsymbol{B}_j - \boldsymbol{I}) - RT\left(\sqrt{(c^{FC})^2 + (c^*)^2} - c^*\right)\boldsymbol{I}. \quad (2.5)$$

The first term represents the background material stiffness of the proteoglycan pools ($\mu^{GAG} = 0.1$ kPa as used previously, which is significantly less than that for elastin) with the left Cauchy–Green tensor defined as $\boldsymbol{B}_j = \boldsymbol{F}_j \boldsymbol{F}_j^T$. The second term accounts for the Gibbs–Donnan swelling pressure caused by the proteoglycans due to the absorption of water into the interstitial space occupied by the GAGs. R and T are the universal gas constant and the absolute body temperature (310 K), c^* is the ionic concentration of the surrounding medium (assumed to be $c^* = 300$ mEq l^{-1}, consistent with prior work), and c^{FC} is the fixed charge density associated with the concentration of GAGs (with $c^* = 200$ mEq l^{-1}, equivalent to approx. 155 kPa Gibbs–Donnan swelling pressure).

With regard to the specific simulations shown below, to account for the change in the *in vivo* axial stretch (from $\lambda_z = 1.4$ at 100 d to $\lambda_z = 1.17$ at 140 d), this stretch was reduced gradually from 1.40 to 1.17 while maintaining quasi-static equilibrium. To simulate different collagen pre-stretches, the adventitial value was increased by 5, 10 or 15% (e.g. from $G_A^{k=1,2,3,4} = 1.25$ in electronic supplementary material, table S8 to $G_A^{k=1,2,3,4} = 1.44$). Similar steps were repeated on the baseline model when increasing the stiffness parameters of the adventitial collagen, as, for example, from $c_1^{k=1,2,3,4} = 59.01$ kPa to $c_1^{k=1,2,3,4} = 885.15$ kPa and from $c_2^{k=1,2,3,4} = 2.934$ to $c_2^{k=1,2,3,4} = 4.70$ (cf. electronic supplementary material, table S8). We also repeated similar steps for an aorta but with normal collagen that simply doubled the adventitia thickness.

2.8. Statistics

Results were tested for normality using the Shapiro–Wilk test and equal variance using Bartlett's test. In groups that failed either of these tests, the non-parametric Kruskal–Wallis test was used to compare results across region, genotype or sex; in groups that passed both of these tests, an analysis of variance (ANOVA) with Bonferroni *post hoc* testing was used. $p < 0.05$ was considered significant.

3. Results

3.1. Systolic cardiac function is normal, but diastolic function becomes compromised

All littermate control (*Lmna*$^{+/+}$ or *Wt*) and progeria (*Lmna*$^{G609G/G609G}$ or *G609G*) mice survived to the intended 140 d of age, though the progeria mice were significantly smaller after approximately 42 d (figure 1*a*): for example, body mass at 140 d was 12.1 ± 0.8 g in female and 13.8 ± 0.9 g in male *G609G* mice compared with 25.0 ± 1.1 g in female and 30.4 ± 2.2 g in male *Wt* mice ($p < 0.01$). The heart was similarly smaller in progeria, yet myocardial microstructure appeared normal histologically (figure 1*b*). *In vivo*

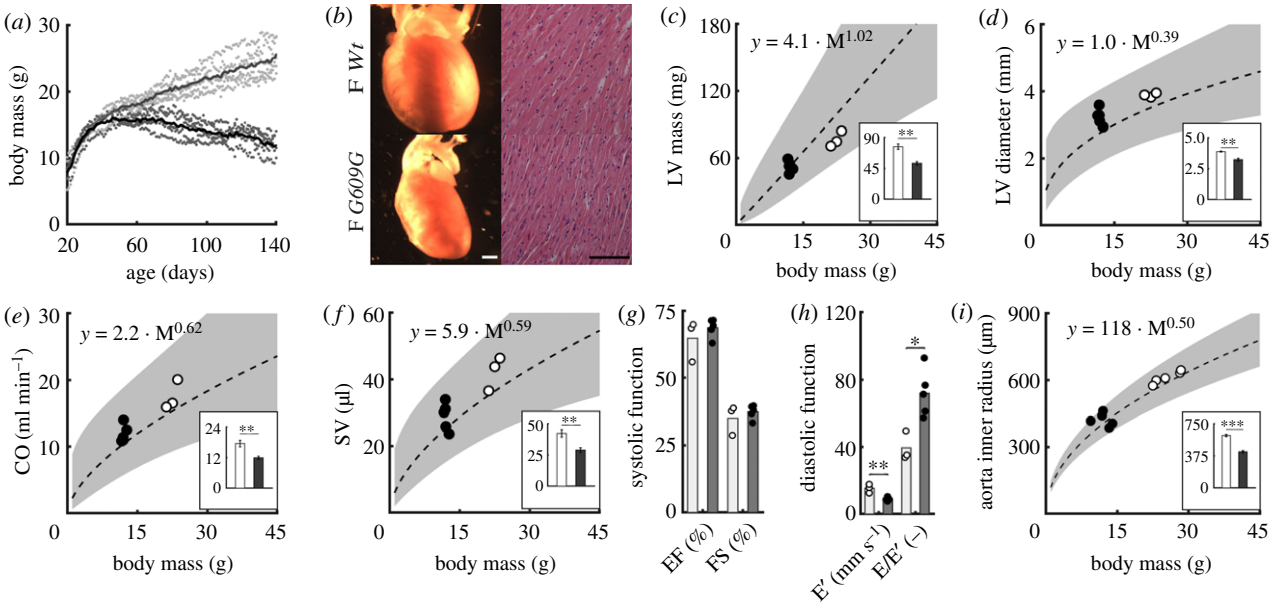

Figure 1. Allometric scaling reveals normal systolic cardiac function despite diastolic dysfunction in 140-day-old female progeria mice. (*a*) Changes in body mass in $Wt = Lmna^{+/+}$ (grey, upper curve) and $G609G = Lmna^{G609G/G609G}$ (black, lower curve) mice from 20 to 140 d. (*b*) Representative images of *Wt* and *G609G* progeria hearts at 140 d, with representative haematoxylin and eosin (H&E) stained cross-sections; scale bars represent 1 mm (white) and 50 µm (black). (*c–f*) Multiple dimensional cardiac metrics (*y*-axes) for 140-day-old progeria mice (dark grey bars, dark grey circles) appear to be statistically lower (subfigure bar-plots, $p < 0.01$) than those for littermate controls (open bars, open circles) until one accounts for body mass, with allometric scaling ($y = cM^k$, with *M* body mass and dashed lines based on data from additional female wild-type controls [19] with 95% prediction interval in grey) revealing nearly appropriate values for the smaller progeria mice: (*c*) left ventricular mass (LV mass), (*d*) LV inner diameter (LV diameter), (*e*) cardiac output (CO) and (*f*) stroke volume (SV). (*g*) Non-dimensional metrics such as ejection fraction (EF) and fractional shortening (FS) confirm normal LV systolic function in 140-day-old progeria mice while (*h*) mitral annular velocity during early filling (E') and the ratio of early transmitral flow velocity *E* to E' (E/E') reveal LV diastolic dysfunction in the same. (*i*) Loaded inner radius of the proximal (descending thoracic) aorta at systolic pressure would also appear to be statistically lower in progeria mice until considered allometrically, hence emphasizing the importance of accounting for the smaller body size in progeria (*a*). ***$p < 0.001$, **$p < 0.01$, *$p < 0.05$.

measurements at 140 d showed that left ventricular mass and diameter, cardiac output, and stroke volume were all significantly lower in progeria (electronic supplementary material, table S1), but these metrics followed allometric scaling with body mass ($y = cM^k$, with *M* body mass and *c* and *k* parameters) indicative of near normal function for a smaller mouse (figure 1*c–f*). Though tail-cuff blood pressure was lower in progeria (electronic supplementary material, figure S1), ejection fraction and fractional shortening were similar between progeria and controls (figure 1*g*), suggesting a preserved systolic function even in the peri-morbid period (*G609G* mice died by approx. 150 d). By contrast, diastolic function was compromised near the end of life. *E* (peak filling velocity in early diastole) and *A* (atrial contraction induced filling velocity in late diastole) were lower in progeria mice at 140 d, with the higher E/A consistent with diastolic dysfunction (electronic supplementary material, table S1). E' was also lower but E/E' was elevated significantly (figure 1*h*), confirming late-stage diastolic dysfunction.

Proximal aortic diameters were also smaller in progeria mice at 140 d, as expected of a smaller mouse, but this metric again followed allometric scaling with body mass (figure 1*i*). Aortic lengths were less in progeria (electronic supplementary material, figure S1), but the time for the pulse pressure wave to travel from the aortic root to the aortic bifurcation was considerably less (electronic supplementary material, figure S1). Consequently, measured PWV was significantly higher in late-stage (140 d) progeria (electronic supplementary material, table S1)—6.16 m s^{-1} versus 3.68 m s^{-1}; $p < 0.001$—suggesting an increased structural stiffness of the progeria aorta consistent with the emerging diastolic dysfunction.

3.2. SMC contractile dysfunction is progressive, becoming extreme in late-stage progeria

The *ex vivo* vasoactive responses were independent of sex at 140 d, hence most data from females and males were combined for clarity of presentation (electronic supplementary material, tables S2 and S3). Both proximal (descending thoracic) and distal (infrarenal abdominal) aortic segments from littermate control mice vasoconstricted strongly to 100 mM KCl and 1 µM PE (figure 2*a–d*), with 10–25% reductions in diameter under physiologically relevant axially isometric (fixed *in vivo* axial stretch) and isobaric (90 mmHg) conditions. By contrast, vasoconstriction was attenuated at 100 d and absent at 140 d in both segments in progeria. Consequently, SMC contraction reduced the mean circumferential wall stress σ_θ ($=Pa/h$, with *P* pressure, *a* luminal radius and *h* wall thickness) by 20–50% in the controls, depending on aortic segment, but not at all at 140 d in progeria (electronic supplementary material, tables S2 and S3). Hence, much-to-all of the haemodynamic loading has to be borne by extracellular matrix in late-stage progeria. Because reduced vasoconstriction could result from a loss of SMCs or compromised cellular contractility, or both, cell number was determined from histology. This quantification confirmed late-stage SMC drop-out (figure 2*e–g*). Vasoconstrictive strength was also normalized by cell number and circumference to account for different vessel calibres by age, region and genotype, which further revealed a reduced ability of the remnant cells to contract in progeria at both 100 d and especially 140 d (figure 2*h*). SMC drop-out thus follows a reduction in function.

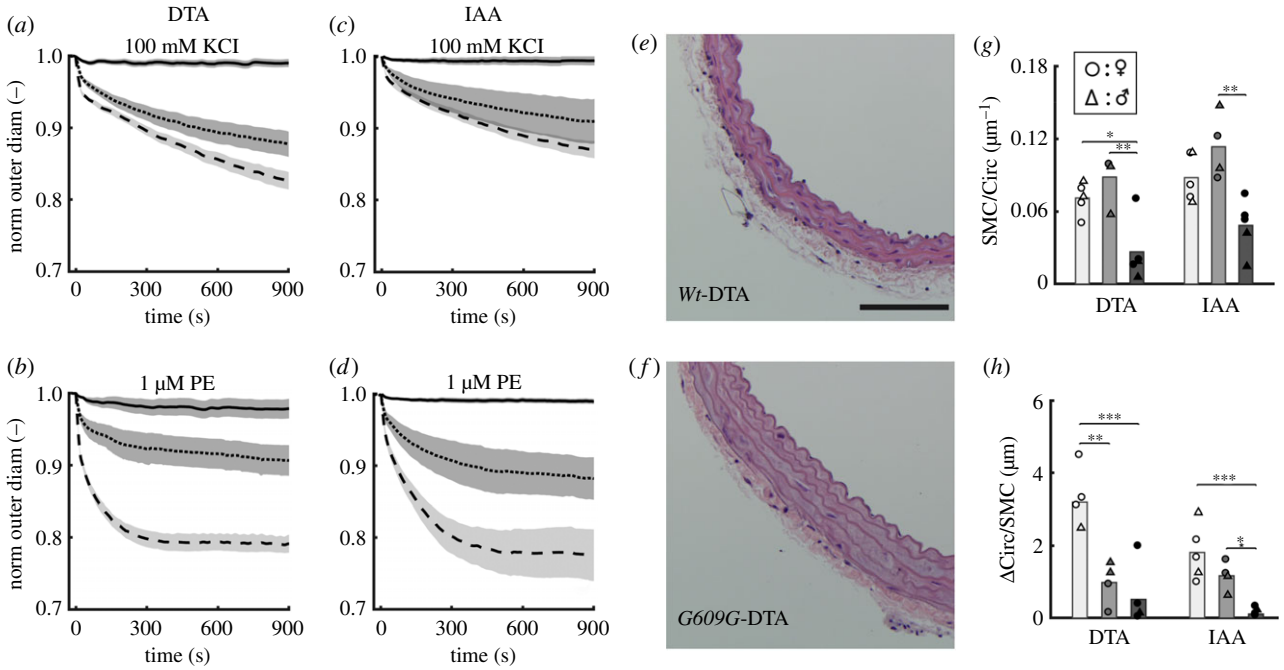

Figure 2. SMC contractile dysfunction is progressive in both the thoracic and abdominal aorta, while SMC drop-out occurs in late-stage progeria. Normalized reduction in outer diameter during *ex vivo* biaxial (isobaric–isometric) vasoconstriction in response to (*a*,*c*) 100 mM KCl (membrane depolarization) or (*b*,*d*) 1 μM PE (GPCR-RhoA-ROCK pathway), at 90 mmHg and group-specific values of *in vivo* axial stretch for the descending thoracic aorta (DTA) and infrarenal abdominal aorta (IAA) from 140-day-old mixed-sex littermate *Wt* (dashed lines) as well as 100- (dotted lines) and 140- (solid lines) day-old progeria mice. (*e*,*f*) Representative histological images of the DTA from 140-day *Wt* (*e*) and *G609G* progeria (*f*) mice stained with haematoxylin and eosin (H&E); the IAA was similar. Scale bar represents 100 μm. (*g*) Cross-sectional smooth muscle cell (SMC) nuclei count normalized by the loaded (90 mmHg and *in vivo* axial stretch) inner circumference for the DTA and IAA for 140-day-old *Wt* (open) and 100- (grey) and 140- (black) day-old female (○) and male (△) progeria mice. (*h*) Change in circumference (distance) per SMC, calculated as $\Delta\mathrm{Circ}/\mathrm{SMC} = \Delta d_{o,\mathrm{act}}/d_o \cdot 2\pi R_i \lambda_\varphi / N_{\mathrm{SMC}}$, where $\Delta d_{o,\mathrm{act}}/d_o$ is the normalized reduction in outer diameter in response to 1 μM PE after 900 s of contraction, $2\pi R_i \lambda_\varphi$ is the loaded inner circumference and N_{SMC} is the SMC nuclei count. Normalization accounts for different sizes at different ages and across genotypes. ***$p < 0.001$, **$p < 0.01$, *$p < 0.05$.

3.3. The aortic biomechanical phenotype is progressive, becoming extreme

Passive geometrical and mechanical data were quantified from *ex vivo* biaxial tests on progeria and age-matched littermate control aortas, both thoracic and abdominal, with data from males and females again similar (electronic supplementary material, tables S4–S7) and thus combined for clarity. Biaxial structural stiffening manifested in the progeria aorta at 100 d, but progressed to extreme stiffening at 140 d (figure 3*a*–*d*) consistent with the measured increase in PWV (electronic supplementary material, table S1). Albeit not shown, all biaxial data (cf. electronic supplementary material, figure S2), progeria and control, were fit well by the same nonlinear constitutive relation; associated best-fit values of the constitutive parameters are in electronic supplementary material, tables S4 and S6. Combined with appropriate geometrical data (electronic supplementary material, tables S5 and S7), these results allow one to compute key metrics such as mean biaxial wall stretch, wall stress and the intrinsic material stiffness (figure 3*e*,*f* and electronic supplementary material, figure S2), and similarly the capacity of the aortic wall to store elastic energy upon deformation (electronic supplementary material, figure S3). Finally, calculations of segmental PWV revealed significant elevations in proximal and especially distal regions in late-stage progeria (figure 3*h*) consistent with elevated measured values (electronic supplementary material, table S1). Whereas decreased circumferential stretch and wall stress were expected because of the marked thickening of the wall in progeria (figure 3*g*), the ubiquitously lower circumferential material stiffness at 100 and 140 d and the progressive decrease in elastic energy storage from 100 to 140 d were extreme. The former reveals that the increased structural stiffness, which increases PWV, results largely from thickening of the wall despite the paradoxical lower intrinsic material stiffness; the latter reveals a marked loss of mechanical functionality in late-stage progeria since a primary mechanical function of the aorta is to store elastic energy during systole and to use this energy during diastole to work on the blood and augment flow.

3.4. Late-stage proteoglycan accumulation is diffuse and dramatic

Aortic properties and function stem from the underlying microstructural composition and architecture. Despite the progressive loss of elastic energy storage capability, the elastic laminae appeared intact throughout the aorta in progeria, though more separated and less undulated at 140 d (figure 4*a*–*d*). The latter appeared to be caused by a dramatic increase in proteoglycans at 140 d in progeria, especially in the media. Immunostaining revealed that, although absent in the controls, aggrecan was the primary proteoglycan within the media in progeria at 140 d (figure 4*e*–*g*). It appears that the strong negative fixed charge density of the proteoglycans and associated Gibbs–Donnan swelling increased the separation of the elastic lamellae and decreased their undulation. Although less dramatic, proteoglycans similarly appeared to thicken the adventitia (not shown) and to decrease the collagen fibre undulation

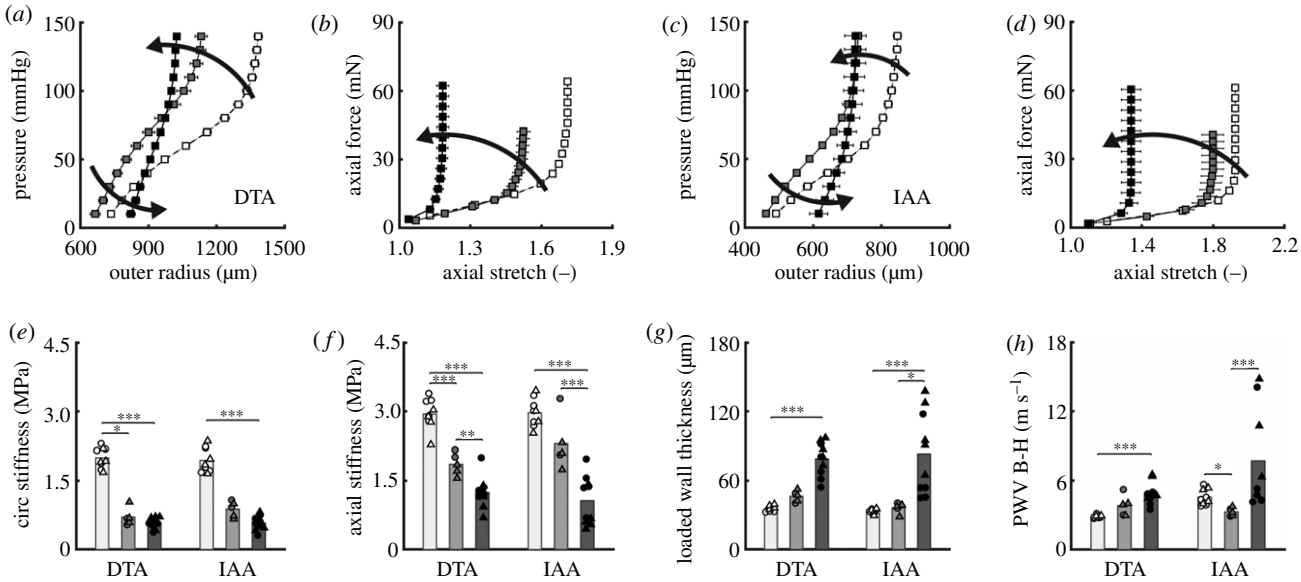

Figure 3. The aortic biomechanical phenotype deteriorates progressively in progeria. Pressure–outer diameter (distensibility) and axial force–stretch (extensibility) relationships for 140-day-old mixed-sex *Wt* (dashed curve, open symbols) as well as 100- (dotted, light grey) and 140- (solid, dark grey) day-old mixed-sex progeria mice reveal a general structural stiffening (left-ward shift) in the physiologic range: (*a*,*b*) descending thoracic aorta (DTA) and (*c*,*d*) infrarenal abdominal aorta (IAA). (*e*–*h*) Representative computed geometrical and mechanical metrics from passive tests on the 140-day-old female (○) and male (△) control (open) and 100- (light grey) and 140- (dark grey) day-old progeria (filled) aortas under *in vivo* systolic conditions. (*e*,*f*) Circumferential and axial material stiffness. (*g*) Loaded wall thickness and (*h*) calculated regional pulse wave velocity using the Bramwell–Hill equation $\mathrm{PWV} = 1/\sqrt{\rho \cdot (\mathrm{d}A/\mathrm{d}P)|_{\mathrm{dias}}/A_{\mathrm{dias}}}$, where ρ is the fluid mass density, A is the luminal cross-section and P is the pressure. ***$p < 0.001$, **$p < 0.01$, *$p < 0.05$.

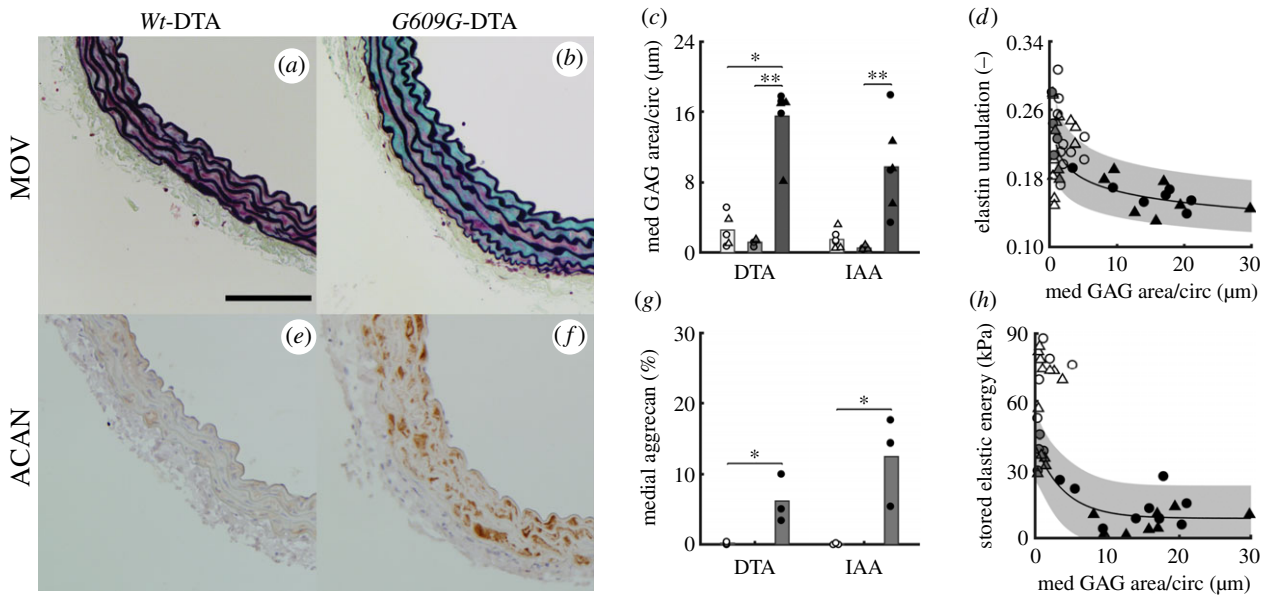

Figure 4. Proteoglycan accumulation is dramatic in late-stage progeria aorta. Histological images of the DTA from 140 d *Wt* and *G609G* progeria mice: Movat (*a*,*b*) and Aggrecan (*e*,*f*). Scale bar represents 100 μm. Images were similar for the IAA. Quantification of (*c*) medial GAG of 140 d *Wt* (open), 100 d *G609G* (grey) and 140 d *G609G* (black) mouse aortas, each normalized by inner vessel circumference at systolic loading conditions to account for different aortic size by region, sex and genotype. (*g*) Fraction of medial aggrecan. (*d*) Elastin fibre undulation (using CT-FIRE) shown as a function of medial GAGs, again normalized by loaded inner circumference at systole. (*h*) Stored elastic energy as a function of medial GAG normalized by inner circumference. The curves are fit to progeria data only. GAG, glycosaminoglycan. ***$p < 0.001$, **$p < 0.01$, *$p < 0.05$.

(electronic supplementary material, figures S4 and S5). Finally, plotting mechanical metrics versus proteoglycan fraction revealed that the dramatically lower circumferential material stiffness manifested before proteoglycan production (not shown), whereas the degree of change from compromised-to-extreme in most other metrics correlated with proteoglycan presence (cf. Figure 4*h* and electronic supplementary material, figure S5), which saturated at contents above approximately 15%.

3.5. Computational modelling reveals roles of accumulated proteoglycans and remodelled collagen

Biological assays such as western blots and (immuno)histochemistry provide critical information on tissue composition and some information on tissue organization, but they cannot reveal functional consequences, which are important clinically. Thus, we used a novel particle-based biomechanical model of the aorta that allows one to delineate constituent-

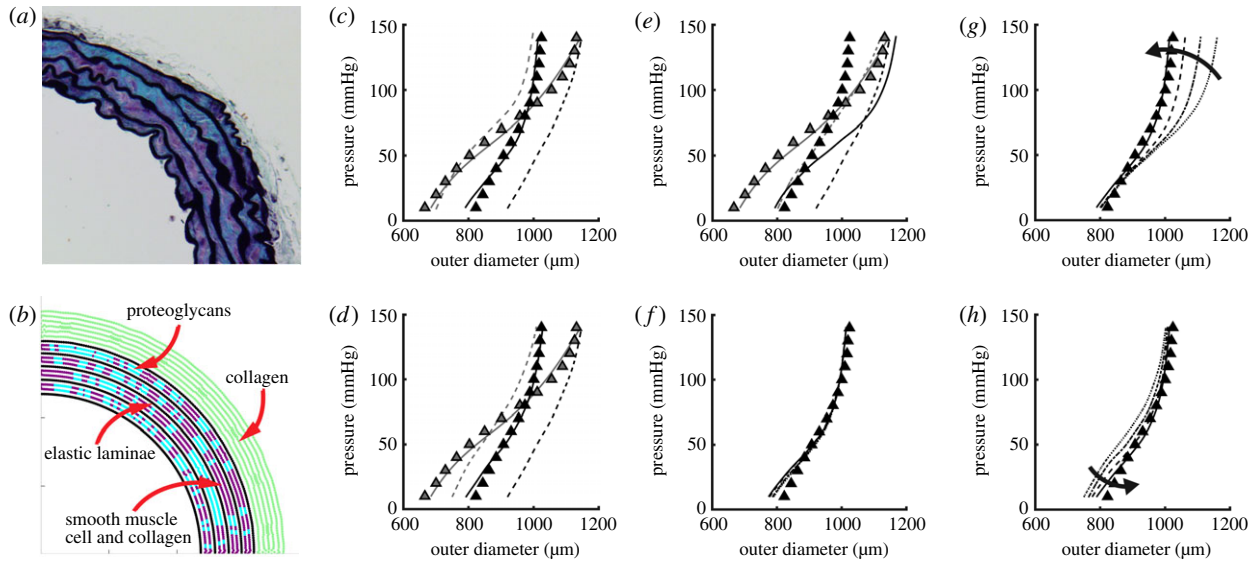

Figure 5. Computational modelling reveals biomechanical roles of accumulated proteoglycans and remodelled collagen. (*a*) Movat-stained descending thoracic aorta (DTA) from a 140-day-old progeria mouse. (*b*) Particle-based computational model of the DTA with stochastic distributions of proteoglycan (blue) between the elastic laminae (black) in the media, with separate mechanical properties prescribed for the primary structural constituents in both the media and adventitia, including Gibbs–Donnan swelling of proteoglycans. (*c*,*d*) Computational results show a good fit to the pressure–diameter response of a 100-day-old progeria DTA (grey ▲, grey curves), as well as the ability of the model to fit data for the 140-day-old progeria DTA (black ▲, black curves) only if combining three factors: the measured decrease in axial stretch (dark dashed), GAGs occupying 30% of the media, and remodelled collagen (light dashed) by changing either collagen (*c*) undulation or (*d*) material properties, but not just (*e*) simply adding more collagen having normal properties to thicken the wall (solid curve) to the measured level. Finally, (*f*) shows that the particular stochastic distribution of the proteoglycans is not critical, whereas the (*g*) degree of change in the collagen remodelling (e.g. 0, 5, 10 and 15% increase in deposition stretch) or the (*h*) addition of more swollen proteoglycans (0, 10, 20 and 30% increases shown) is essential for fitting well the experimental data.

specific consequences of compositional and organizational changes [25]. Figure 5*a* shows a histologically defined cross-section of the unloaded DTA from a progeria mouse, while figure 5*b* shows a general computational model of the same; see also electronic supplementary material, table S8 for model parameters. The control model (not shown) was endowed with properties consistent with health; the 140 d progeria model included a modified medial layer that contained five intact, nearly straight elastic laminae with dysfunctional intra-lamellar SMCs (no contractility), remodelled fibrillar collagen, and excessive stochastically distributed proteoglycans plus an adventitial layer that consisted primarily of remodelled fibrillar collagen with little proteoglycan. Individual 'particles' within each computational model allowed fine spatial resolution (approx. 2 µm in the pressurized state) and enabled the different constituents to interact physically.

Figure 5*c*,*d* shows the ability of this model (lines) to describe pressure–diameter data (filled Δ) at group-specific fixed axial stretches for both 100 d (structurally more compliant; grey, dashed lines) and 140 d (structurally stiffer; black, solid lines) progeria aorta. Consistent with histological assessments, the model fit the control and different progeria data assuming the same amount and properties of the elastic lamellae, noting that straightening the elastic laminae has little effect on stiffness because of their nearly linear stress-stretch behaviour [15]. Importantly, the model could only fit the 140 d progeria data when introducing three modifications relative to the 100 d progeria data: a marked reduction in the *in vivo* axial stretch (from 1.4 to 1.17), which was measured directly (electronic supplementary material, tables S5 and S7), a marked increase (from approx. 0 to 32% of the media) in highly negatively charged medial proteoglycans (figure 4), and marked remodelling of adventitial collagen, consistent with either the observed loss of undulation (electronic supplementary material, figures S4 and S5) or change in material stiffness (figure 3). Simulations with reduced axial stretch alone and similarly remodelled collagen alone showed that these effects were not sufficient individually; rather all three changes needed to coexist to capture the structurally stiffer behaviour (solid line). Similarly, simply increasing the thickness of the collagen-rich adventitia with normal collagen could not describe the 140 d data (figure 5*e*). Finally, figure 5*f* shows that it was not the specific (stochastic) distribution of the proteoglycans that mattered, but rather the associated degree of collagen remodelling (figure 5*g*) plus the proteoglycan accumulation (figure 5*h*) at 140 d.

3.6. Comparisons against normal ageing and disease highlight the late-stage severity of progeria

Electronic supplementary material, figures S7 and S8, compare key biomechanical metrics at group-specific systolic pressures for the DTA of male mice across four different mouse models—naturally aged, two with compromised elastic fibre integrity and induced hypertension. Note the consistency across controls for different ages of normal young adults, namely 56, 84 and 140 d old C57BL/6 mice, particularly compared with 350 and 700 d old mice that aged naturally [17] and the 100 and 140 d old progeria ($Lmna^{G609G/G609G}$) mice (electronic supplementary material, figure S7). The 140 d progeria mice exhibited the most dramatic phenotype across all metrics, but interestingly the 100 d progeria mice shared many similarities with the 700 d old naturally aged mice, especially wall thickness, distensibility, extensibility and energy storage, though not material stiffness, which was consistently lower in progeria. Albeit not shown, the control groups at 56–140 d old

were very similar to 140 d old littermate controls ($Lmna^{+/+}$), which were used for comparison. Thus consider direct comparisons of aortic data for 700 d old naturally aged (repeated) mice as well as 56 and 90 d old Marfan syndrome ($Fbn1^{mgR/mgR}$) mice [22], 140 d old fibulin-5 deficient ($Fbln5^{-/-}$) mice [20] and 84 d old angiotensin II infusion induced hypertensive C57BL/6 mice [23]—again versus 100 and 140 d progeria data (electronic supplementary material, figure S8). The 140 d progeria aortas again exhibited the most severe phenotype of all models, particularly with dramatic reductions in biaxial wall stretch (i.e. reduced distension and extension, consistent with increased structural stiffness), wall stress and material stiffness. Only the reduced elastic energy storage in the induced hypertension model approached that of the 140 d progeria aorta, noting that these hypertensive aortas thickened dramatically due to adventitial fibrosis and thus result from different microstructural changes (cf. Figure 4 and electronic supplementary material, figures S4 and S5). Albeit not shown, the contractile response to high KCl or PE was also lowest in the 140 d progeria aorta of all of the models compared (*Wt*, fibulin-5 null and induced hypertension), consistent with a previously reported low contractile protein expression in progeria [12].

4. Discussion

HGPS is an ultra-rare disorder, presenting in 1 out of 4–8 million live births. Because patient data are scant, mouse models provide critical insight into the natural history of this devastating syndrome as well as into mechanisms and manifestations of vascular ageing in general. There are numerous reports of central artery ageing in wild-type mice. A comparison of six- versus 20-month-old C57BL/6 mice revealed 1503 differentially expressed genes in the thoracic aorta, with significant differences in calcium handling, extracellular matrix and cell adhesion as well as increased (23%) aortic PWV with consequent increased (17%) central blood pressure [26]. Structural stiffening of normally aged murine arteries has been ascribed largely to adventitial fibrosis [27], and adventitial thickening manifests in the c.1824C>T;p.G608G transgenic mouse model of progeria [11] and in some [28] though not all [15] central arteries in $Lmna^{G609G/G609G}$ mice. Although clinical phenotypes are often associated with gene expression or histological findings, one must also quantify associated functional metrics that define the aortic phenotype, which ultimately governs cardiovascular health and disease risk [29,30]. Although it has long been speculated that mechanical stress plays a key role in progeria [1,11,28], there had not yet been any detailed biaxial biomechanical analyses, particularly in the peri-morbid period.

It was instructive to compare the present biomechanical results directly with those for normal ageing [17] as well as with those for compromised elastic fibre integrity [20,22], a feature common in aortic ageing, and those for hypertension [23,31], which often associates with ageing. Remarkably, the progeria phenotype at 100 d was similar to that of both elastic fibre compromised and naturally aged (to 700 d) aortas, indicative of highly accelerated ageing in progeria. Nonetheless, there was a dramatic worsening of the cardiovascular state from 100 to 140 d in progeria, consistent with the histological appearance of extensive proteoglycans, resulting in an aortic biomechanical phenotype that was extreme relative to natural ageing, severe elastopathies and hypertension, each of which also increase PWV and compromise diastolic heart function. Although aortic thickening was most dramatic in angiotensin II-induced hypertension, the associated reduction in wall stress σ_θ was greatest (approx. 75%) in the 140 d progeria aorta (figure 3) due to the combination of lower blood pressure, smaller lumen and markedly thickened wall (recall $\sigma_\theta = Pa/h$). Reduced peripheral blood pressure excluded hypertension as a driver of the phenotype. Importantly, allometric scaling [32] revealed that the smaller lumen was appropriate for the smaller mice having reduced cardiac output (figure 1), hence excluding pathologic inward remodelling in progeria though suggested elsewhere [15]. The greater reduction in axial (pre)stretch in progeria (approx. 28%; electronic supplementary material, tables S5 and S7) also contributed to these differences, emphasizing the need for biaxial measurements, which had not been performed in detail before. Axial pre-stretch normally arises in arteries due to perinatal deposition and cross-linking of elastic fibres having a long half-life, but increases in other matrix constituents can reduce its extent in maturity. Notably, dramatic increases in intramural proteoglycans late in progeria contributed to both wall thickening and the reduced axial recoil, which computational modelling revealed as fundamental to the marked alterations in wall mechanics (figure 5).

We previously showed that decreases in elastic energy storage upon pressurization reflect a loss of mechanical functionality of the aorta [20], which should store energy during systole for use during diastole to work on the blood [33]. Such decreases are common in cases of compromised elastic fibre integrity and hypertension [22,31], though for different reasons—an inability to store energy in impaired elastic fibres in the former and an inability to distend competent elastic fibres in the latter. Remarkably, despite preserved elastic laminae (figure 4), the 140 d progeria aorta exhibited the greatest loss of energy storage capability of all models compared (electronic supplementary material, figures S7 and S8). The associated reduced distensibility of the structurally stiffer wall, and thus inability to deform the elastic fibres, again appeared to result primarily from the excessive intramural proteoglycans at 140 d (figures 4 and 5). Critically, an extreme loss of energy storage by the proximal aorta would compromise diastolic cardiac function further, for energy stored in this segment can help lift the base of the heart and promote diastolic filling [19]. Whereas increased circumferential material stiffness correlates with thoracic aortic aneurysm, as in Marfan syndrome [22,32], perhaps most notable herein was its dramatically lower value in the 100 and 140 d progeria aortas. An inability to control circumferential stiffness appears to reflect a compromised ability of the intramural cells to mechano-sense and mechano-regulate their local mechanical environment [34], consistent with observed changes in matrix and adhesion molecule gene expression in natural ageing [26]. Importantly, the markedly lower intrinsic aortic stiffness in progeria is also consistent with the finding that normal levels of lamin A scale with tissue stiffness [10]. Whereas prior reports show that decreased material stiffness of the surrounding matrix can drive lower lamin A in normal cells, our findings suggest further that loss of normal lamin A or presence of progerin can compromise mechanical homeostasis and manifest as a lower material stiffness of the matrix. It is thus critical to delineate intrinsic material stiffness and overall structural stiffness (figure 3) [15], the latter of which results from a combination of material stiffness and wall thickness and ultimately affects the haemodynamics. That progeria

results in a greater structural stiffness with a paradoxically reduced material stiffness seems consistent with consequences of a *Lmna* mutation as well as the consequent geometric changes and clinical phenotype. Continued research should nevertheless focus on the biological processes by which the intrinsic material stiffness remains so low in progeria.

Recalling that progeria patients exhibit increased PWV [2], the diffusely increased local structural stiffness in the 140 d progeria aortas (figure 3) manifested globally as an increased PWV (6.2 m s^{-1} late in progeria; electronic supplementary material, table S1), which was greater than that in severe elastopathy (4.5 m s^{-1} in fibulin-5 deficiency [35]) and normal murine ageing (3.8 m s^{-1} [26]), all relative to control (approx. 3.0–3.3 m s^{-1}). That PWV increased despite the marked reduction in circumferential material stiffness again highlights the important structural effect of wall thickening, particularly when combined with an allometrically reduced luminal calibre (recall the Moens–Korteweg equation, PWV $\sim \sqrt{Eh/2\rho a}$, with E a tensile material stiffness, h wall thickness, a luminal radius and ρ blood viscosity [35]). That computed values of PWV differed by aortic region emphasizes the need for regional studies of the biomechanics while highlighting the importance of local mechanobiology on global physiology [30], which in this case manifested as a compromised diastolic cardiac function (figure 1). Although our measured and calculated values of PWV were consistent, there is a need for more rigorous regional calculations using image-based three-dimensional simulations via fluid–solid interaction models. There is similarly a need for detailed computational studies of the ventricular–vascular coupling.

It was somewhat remarkable that systolic function was largely preserved, even in the peri-morbid period (140 d), consistent with the original report for the $Lmna^{G609G/G609G}$ mice at a younger (103 d) age [13]. We emphasize two important points here. First, because of the significantly smaller body mass M in progeria after about 42 d (figure 1*a*), allometric scaling ($y = cM^k$) is essential when assessing dimensioned cardiovascular metrics [32], including cardiac output, stroke volume and aortic dimensions, each of which would otherwise appear to be statistically lower in progeria and yet were appropriate for the smaller mice. Interestingly, our best-fit allometric parameters k are comparable to those in other rodents [36] as well as some humans [37,38]. We submit, therefore, that allometric (or similar) scaling should be used when interpreting cardiovascular data in progeria due to the growth retardation. Toward this end, additional data on wild-type male and female mice should be collected over broader ages and thus ranges of body mass for different backgrounds. Second, recalling that diastolic dysfunction manifests in progeria patients [5], the impaired diastolic function in the 140 d progeria mice (trend toward higher E/A and statistically higher E/E') may have been underestimated due to the anaesthesia during echocardiography. Such cardiac deficits could be exacerbated by physical exertion, perhaps explaining the progressively sedentary lifestyle of these mice. Collection of *in vivo* data under non-anesthetized conditions is difficult, but would provide increased insight.

We quantified absolute histological changes but normalized values by luminal circumference to account for differences in calibre due to age, sex, body size, genotype and location along the aorta. Considered in this way, the density of elastic laminae dropped from 100 to 140 d in progeria, consistent with increases in collagen and especially proteoglycans, but remained higher than in *Wt*, likely due to the allometrically smaller lumen. Thus, loss of energy storage capability was not due to compromised elastin. These as well as our computational findings thus suggest that the adverse aortic remodelling began after the developmental period when elastin is deposited and matured [33], which is typically assumed to occur by weaning. Given the lower blood pressures and thus lower wall stress and stiffness during development, it seems that the SMCs initially fashioned appropriate elastic fibre integrity, consistent with the lack of any phenotype in compliant, low-stressed organs in progeria (e.g. brain and liver [28]). By contrast, collagen turns over continuously [39]. Collagen density remained nearly normal in progeria (electronic supplementary material, figure S5), yet later turnover of initially normal collagen in the face of higher blood pressures in maturity could explain some of the progressive worsening of the aortic phenotype, recalling that the computational model predicted that the observed collagen had to differ mechanically in late-stage progeria in order for the model to capture the measured data. Although the reduced undulation of adventitial fibres (electronic supplementary material, figures S4 and S5) might have been expected to increase material stiffness, the thickened media likely stress shielded these fibres at normal pressures [40], though they could yet help prevent overall dilatation, noting that aneurysms have not been reported in progeria. That the proteoglycans thickened the media, separating the elastic lamellae via Gibbs–Donnan swelling, could have compromised SMC mechano-sensing further [41], thus adversely affecting matrix remodelling and cell adhesion [26] and perhaps inducing cell death via anoikis [42]. There is clearly a need for more information on progressive changes in cell–matrix interactions and SMC signalling in progeria. Associated aortic consequences could be greater at higher haemodynamic loads, thus future studies of the effects of exercise on these progeria mice at different ages could be very informative.

When appropriately normalized, histology also suggested that the lost vasoconstriction in the peri-morbid period (figure 2*a–d*) resulted both from the previously reported SMC drop-out [14] and the new finding that the contractile capacity was lower per remnant cell, mainly for PE, an alpha1-adrenergic agonist. PE mediates contraction through the RhoA-ROCK pathway, consistent with reports of reduced RhoA activity in HGPS mice and the hypothesis that a disrupted LINC complex correlates with weakened cell–matrix adhesion [43]. Reduced central artery contractility manifests in many conditions, including Marfan syndrome [44], fibulin-5 deficiency [21], induced hypertension [31] and natural aortic ageing [45]. Yet, vascular contractility is only attenuated, not absent, in these other cases. Varga *et al.* [11] previously reported diminished *in vivo* vasodilation to sodium nitroprusside in the transgenic c.1824C>T;pG608G mouse, while Capell *et al.* [12] reported a decrease in SM-α actin, yet ours is the first report of a total, late-stage loss of vasoconstrictive capacity under physiological conditions. Reduced vessel-level contractility compromises the ability of the cells to maintain or appropriately remodel the wall in response to haemodynamic loads [46,47]. Reduced vasoconstriction also suggests a loss of cell-tissue level actomyosin activity, which is needed to mechano-sense and mechano-regulate the extracellular matrix [34]. It should not escape one's notice, therefore, that the altered nuclear stiffness, severely diminished actomyosin activity, and compromised extracellular matrix in progeria lie along the

mechanotransduction axis, suggesting that progressive microstructural changes follow a worsening ability of the SMCs to remodel or repair the matrix in a highly stressed environment, resulting in excessive proteoglycan production, particularly aggrecan which is typically not found in the aorta (cf. [48]) though it is produced by dermal fibroblasts in HGPS [49].

Increased PWV, reflective of central artery stiffening, has emerged as characteristic of the systemic vasculature in progeria [2,5,50]. Such structural stiffening in the general population is predictive of future cardiovascular events, including myocardial infarction, stroke and heart failure [3,4], and may be an indicator of premature vascular ageing [51]. Our findings revealed highly accelerated aortic ageing in progeria up to 100 d, comparable to that of extreme natural ageing and genetically compromised elastic fibre integrity in mice, followed by an extreme late-stage (100–140 d) loss of aortic contractile and biomechanical function, independent of sex, leading to significant increases in structural stiffness and PWV despite a paradoxically low intrinsic material stiffness consistent with the lamin A mutation and indicative of compromised mechanical homeostasis. Because the aortic phenotype and associated cardiac performance are much less severe at 100 d [13] than in peri-morbid 140 d progeria mice (figures 1–3), there may be a late therapeutic window that could expand treatment options to drugs that otherwise would be questioned due to growth restriction in children (cf. [52]). In particular, it would be prudent to control SMC phenotype and limit proteoglycan accumulation, which appear to drive the extreme central artery stiffening and devastating cardiovascular sequelae in HGPS.

Disclosures

D.T.B. is an equity holder in, and receives research and consulting support from, Inozyme Pharma, Inc. for therapeutics for ENPP1 deficiency. None of the other authors declare any conflict, financial or otherwise.

Data accessibility. Dataset available from the Dryad Digital Repository: https://dx.doi.org/10.5061/dryad.mcvdncjw9 [53].

Authors' contributions. S.-I.M., D.T.B. and J.D.H. designed the research; S.-I.M., Y.K., A.W.C., H.A., N.M., K.Z., D.K., D.W., M.L. and Z.W.Z. performed the research; S.-I.M., Y.K., H.A., D.K., D.T.B. and J.D.H. analysed the data; G.S.S. contributed new reagents or tools; S.-I.M. and J.D.H. wrote the paper.

Competing interests. We declare we have no competing interests.

Funding. This work was supported, in part, by grants from the US National Institutes of Health: R01 HL105297 (J.D.H.) and P01 HL134605 (Dan Rifkin) and R01 AG047632 and R33 ES025636 (G.S.S.).

Acknowledgements. We acknowledge expert technical advice from Drs Jacopo Ferruzzi and Bart Spronck, Yale University.

References

1. Olive M *et al.* 2010 Cardiovascular pathology in Hutchinson–Gilford progeria: correlation with the vascular pathology of aging. *Arterioscler. Thromb. Vasc. Biol.* **30**, 2301–2309. (doi:10.1161/ATVBAHA.110.209460)
2. Gerhard-Herman M *et al.* 2012 Mechanisms of premature vascular aging in children with Hutchinson–Gilford progeria syndrome. *Hypertension* **59**, 92–97. (doi:10.1161/HYPERTENSIONAHA.111.180919)
3. Vlachopoulos C, Aznaouridis K, Stefanadis C. 2010 Prediction of cardiovascular events and all-cause mortality with arterial stiffness: a systematic review and meta-analysis. *J. Am. Coll. Cardiol.* **55**, 1318–1327. (doi:10.1016/j.jacc.2009.10.061)
4. Mitchell GF, Hwang S-J, Vasan RS, Larson MG, Pencina MJ, Hamburg NM, Vita JA, Levy D, Benjamin EJ. 2010 Arterial stiffness and cardiovascular events: the Framingham Heart Study. *Circulation* **121**, 505. (doi:10.1161/CIRCULATIONAHA.109.886655)
5. Prakash A *et al.* 2018 Cardiac abnormalities in patients with Hutchinson–Gilford progeria syndrome. *JAMA Cardiol.* **3**, 326–334. (doi:10.1001/jamacardio.2017.5235)
6. Gordon LB, Shappell H, Massaro J, D'Agostino RB, Brazier J, Campbell SE, Kleinman ME, Kieran MW. 2018 Association of lonafarnib treatment vs no treatment with mortality rate in patients with Hutchinson–Gilford progeria syndrome. *J. Am. Med. Assoc.* **319**, 1687–1695. (doi:10.1001/jama.2018.3264)
7. Eriksson M *et al.* 2003 Recurrent de novo point mutations in lamin A cause Hutchinson–Gilford progeria syndrome. *Nature* **423**, 293. (doi:10.1038/nature01629)
8. De Sandre-Giovannoli A *et al.* 2003 Lamin A truncation in Hutchinson–Gilford progeria. *Science* **300**, 2055. (doi:10.1126/science.1084125)
9. Verstraeten VL, Ji JY, Cummings KS, Lee RT, Lammerding J. 2008 Increased mechanosensitivity and nuclear stiffness in Hutchinson–Gilford progeria cells: effects of farnesyltransferase inhibitors. *Aging Cell* **7**, 383–393. (doi:10.1111/j.1474-9726.2008.00382.x)
10. Swift J *et al.* 2013 Nuclear lamin-A scales with tissue stiffness and enhances matrix-directed differentiation. *Science* **341**, 1240104. (doi:10.1126/science.1240104)
11. Varga R *et al.* 2006 Progressive vascular smooth muscle cell defects in a mouse model of Hutchinson–Gilford progeria syndrome. *Proc. Natl Acad. Sci. USA* **103**, 3250–3255. (doi:10.1073/pnas.0600012103)
12. Capell BC *et al.* 2008 A farnesyltransferase inhibitor prevents both the onset and late progression of cardiovascular disease in a progeria mouse model. *Proc. Natl Acad. Sci. USA* **105**, 15 902–15 907. (doi:10.1073/pnas.0807840105)
13. Osorio FG *et al.* 2011 Splicing-directed therapy in a new mouse model of human accelerated aging. *Sci. Transl. Med.* **3**, 106ra107. (doi:10.1126/scitranslmed.3002847)
14. Villa-Bellosta R, Rivera-Torres J, Osorio FG, Acín-Pérez R, Enriquez JA, López-Otín C, Andrés V. 2013 Defective extracellular pyrophosphate metabolism promotes vascular calcification in a mouse model of Hutchinson–Gilford progeria syndrome that is ameliorated on pyrophosphate treatment. *Circulation* **127**, 2442–2451. (doi:10.1161/CIRCULATIONAHA.112.000571)
15. Del Campo L *et al.* 2019 Vascular smooth muscle cell-specific progerin expression in a mouse model of Hutchinson–Gilford progeria syndrome promotes arterial stiffness: therapeutic effect of dietary nitrite. *Aging Cell* **18**, e12936. (doi:10.1111/acel.12936)
16. Rogers WJ, Hu YL, Coast D, Vido DA, Kramer CM, Pyeritz RE, Reichek N. 2001 Age-associated changes in regional aortic pulse wave velocity. *J. Am. Coll. Cardiol.* **38**, 1123–1129. (doi:10.1016/S0735-1097(01)01504-2)
17. Ferruzzi J, Madziva D, Caulk AW, Tellides G, Humphrey JD. 2018 Compromised mechanical homeostasis in arterial aging and associated cardiovascular consequences. *Biomech. Model. Mechanobiol.* **17**, 1281–1295. (doi:10.1007/s10237-018-1026-7)
18. Kreienkamp R *et al.* 2019 Doubled lifespan and patient-like pathologies in progeria mice fed high-fat diet. *Aging Cell* **18**, e12852. (doi:10.1111/acel.12852)
19. Ferruzzi J, Di Achille P, Tellides G, Humphrey JD. 2018*b* Combining *in vivo* and *in vitro* biomechanical data reveals key roles of perivascular tethering in central artery function. *PLoS ONE* **13**, e0201379. (doi:10.1371/journal.pone.0201379)
20. Ferruzzi J, Bersi MR, Uman S, Yanagisawa H, Humphrey JD. 2015 Decreased elastic energy

storage, not increased material stiffness, characterizes central artery dysfunction in fibulin-5 deficiency independent of sex. *J. Biomech. Eng.* **137**, 031007. (doi:10.1115/1.4029431)

21. Murtada SI, Ferruzzi J, Yanagisawa H, Humphrey JD. 2016 Reduced biaxial contractility in the descending thoracic aorta of fibulin-5 deficient mice. *J. Biomech. Eng.* **138**, 051008. (doi:10.1115/1.4032938)
22. Bellini C *et al.* 2017 Comparison of 10 murine models reveals a distinct biomechanical phenotype in thoracic aortic aneurysms. *J. R. Soc. Interface* **14**, 20161036. (doi:10.1098/rsif.2016.1036)
23. Bersi MR, Bellini C, Wu J, Montaniel KR, Harrison DG, Humphrey JD. 2016 Excessive adventitial remodeling leads to early aortic maladaptation in angiotensin-induced hypertension. *Hypertension* **67**, 890–896. (doi:10.1161/HYPERTENSIONAHA.115.06262)
24. Bredfeldt JS *et al.* 2014 Computational segmentation of collagen fibers from second-harmonic generation images of breast cancer. *J. Biomed. Opt.* **19**, 016007. (doi:10.1117/1.JBO.19.1.016007)
25. Ahmadzadeh H, Rausch MK, Humphrey JD. 2018 Particle-based computational modelling of arterial disease. *J. R. Soc. Interface* **15**, 20180616. (doi:10.1098/rsif.2018.0616)
26. Rammos C, Hendgen-Cotta UB, Deenen R, Pohl J, Stock P, Hinzmann C, Kelm M, Rassaf T. 2014 Age-related vascular gene expression profiling in mice. *Mech. Ageing Dev.* **135**, 15–23. (doi:10.1016/j.mad.2014.01.001)
27. Fleenor BS, Marshall KD, Durrant JR, Lesniewski LA, Seals DR. 2010 Arterial stiffening with ageing is associated with transforming growth factor-β1-related changes in adventitial collagen: reversal by aerobic exercise. *J. Physiol.* **588**, 3971–3982. (doi:10.1113/jphysiol.2010.194753)
28. Kim PH *et al.* 2018 Disrupting the LINC complex in smooth muscle cells reduces aortic disease in a mouse model of Hutchinson–Gilford progeria syndrome. *Sci. Trans. Med.* **10**, eaat7163. (doi:10.1126/scitranslmed.aat7163)
29. Laurent S, Boutouyrie P. 2015 The structural factor of hypertension: large and small artery alterations. *Circ. Res.* **116**, 1007–1021. (doi:10.1161/CIRCRESAHA.116.303596)
30. Humphrey JD, Harrison DG, Figueroa CA, Lacolley P, Laurent S. 2016 Central artery stiffness in hypertension and aging: a problem with cause and consequence. *Circ. Res.* **118**, 379–381. (doi:10.1161/CIRCRESAHA.115.307722)
31. Korneva A, Humphrey JD. 2018 Maladaptive aortic remodeling in hypertension associates with dysfunctional smooth muscle contractility. *Am. J. Physiol. Heart Circ. Physiol.* **316**, H265–H278. (doi:10.1152/ajpheart.00503.2017)
32. Korneva A, Zilberberg L, Rifkin DB, Humphrey JD, Bellini C. 2019 Absence of LTBP-3 attenuates the aneurysmal phenotype but not spinal effects on the aorta in Marfan syndrome. *Biomech. Model. Mechanobiol.* **18**, 261–273. (doi:10.1007/s10237-018-1080-1)
33. Wagenseil JE, Mecham RP. 2009 Vascular extracellular matrix and arterial mechanics. *Physiol. Rev.* **89**, 957–989. (doi:10.1152/physrev.00041.2008)
34. Humphrey JD, Schwartz MA, Tellides G, Milewicz DM. 2015 Role of mechanotransduction in vascular biology: focus on thoracic aortic aneurysms and dissections. *Circ. Res.* **116**, 1448–1461. (doi:10.1161/CIRCRESAHA.114.304936)
35. Cuomo F, Ferruzzi J, Agarwal P, Li C, Zhuang ZW, Humphrey JD, Figueroa CA. 2019 Sex-dependent differences in central artery haemodynamics in normal and fibulin-5 deficient mice: implications for ageing. *Proc. R. Soc. A* **475**, 20180076. (doi:10.1098/rspa.2018.0076)
36. White L, Haines H, Adams T. 1968 Cardiac output related to body weight in small mammals. *Comp. Biochem. Physiol.* **27**, 559–565. (doi:10.1016/0010-406X(68)90252-1)
37. de Simone G, Devereux RB, Daniels SR, Mureddu GF, Roman MJ, Kimball TR, Greco R, Witt S, Contaldo F. 1997 Stroke volume and cardiac output in normotensive children and adults: assessment of relations with body size and impact of overweight. *Circulation* **95**, 1837–1843. (doi:10.1161/01.CIR.95.7.1837)
38. Dewey FE, Rosenthal D, Murphy Jr DJ, Froelicher VF, Ashley EA. 2008 Does size matter? Clinical applications of scaling cardiac size and function for body size. *Circulation* **117**, 2279–2287. (doi:10.1161/CIRCULATIONAHA.107.736785)
39. Valentín A, Humphrey JD. 2009 Modeling effects of axial extension on arterial growth and remodeling. *Med. Biol. Eng. Comput.* **47**, 979–987. (doi:10.1007/s11517-009-0513-5)
40. Bellini C, Ferruzzi J, Roccabianca S, Di Martino ES, Humphrey JD. 2014 A microstructurally motivated model of arterial wall mechanics with mechanobiological implications. *Ann. Biomed. Eng.* **42**, 488–502. (doi:10.1007/s10439-013-0928-x)
41. Roccabianca S, Bellini C, Humphrey JD. 2014 Computational modelling suggests good, bad and ugly roles of glycosaminoglycans in arterial wall mechanics and mechanobiology. *J. R. Soc. Interface* **11**, 20140397. (doi:10.1098/rsif.2014.0397)
42. Meredith Jr JE, Fazeli B, Schwartz MA. 1993 The extracellular matrix as a cell survival factor. *Mol. Biol. Cell* **4**, 953–961. (doi:10.1091/mbc.4.9.953)
43. Hale CM, Shrestha AL, Khatau SB, Stewart-Hutchinson PJ, Hernandez L, Stewart CL, Hodzic D, Wirtz D. 2008 Dysfunctional connections between the nucleus and the actin and microtubule networks in laminopathic models. *Biophys. J.* **95**, 5462–5475. (doi:10.1529/biophysj.108.139428)
44. Eberth JF, Taucer AI, Wilson E, Humphrey JD. 2009 Mechanics of carotid arteries in a mouse model of Marfan syndrome. *Ann. Biomed. Eng.* **37**, 1093–1104. (doi:10.1007/s10439-009-9686-1)
45. Wheeler JB, Mukherjee R, Stroud RE, Jones JA, Ikonomidis JS. 2015 Relation of murine thoracic aortic structural and cellular changes with aging to passive and active mechanical properties. *J. Am. Heart Assoc.* **3**, e001744. (doi:10.1161/JAHA.114.001744)
46. Dajnowiec D, Langille BL. 2007 Arterial adaptations to chronic changes in haemodynamic function: coupling vasomotor tone to structural remodelling. *Clin. Sci.* **113**, 15–23. (doi:10.1042/CS20060337)
47. Valentin A, Cardamone L, Baek S, Humphrey JD. 2008 Complementary vasoactivity and matrix remodelling in arterial adaptations to altered flow and pressure. *J. R. Soc. Interface* **6**, 293–306. (doi:10.1098/rsif.2008.0254)
48. Cikach FS *et al.* 2018 Massive aggrecan and versican accumulation in thoracic aortic aneurysm and dissection. *JCI Insight* **3**, e97167. (doi:10.1172/jci.insight.97167)
49. Lemire JM, Patis C, Gordon LB, Sandy JD, Toole BP, Weiss AS. 2006 Aggrecan expression is substantially and abnormally upregulated in Hutchinson–Gilford progeria syndrome dermal fibroblasts. *Mech. Ageing. Dev.* **127**, 660–669. (doi:10.1016/j.mad.2006.03.004)
50. Gordon LB *et al.* 2012 Clinical trial of a farnesyltransferase inhibitor in children with Hutchinson–Gilford progeria syndrome. *Proc. Natl Acad. Sci. USA* **109**, 16 666–16 671. (doi:10.1073/pnas.1202529109)
51. Nilsson PM, Boutouyrie P, Cunha P, Kotsis V, Narkiewicz K, Parati G, Rietzschel E, Scuteri A, Laurent S. 2013 Early vascular ageing in translation: from laboratory investigations to clinical applications in cardiovascular prevention. *J. Hypert.* **31**, 1517–1526. (doi:10.1097/HJH.0b013e328361e4bd)
52. DuBose AJ, Lichtenstein ST, Petrash NM, Erdos MR, Gordon LB, Collins FS. 2018 Everolimus rescues multiple cellular defects in laminopathy-patient fibroblasts. *Proc. Natl Acad. Sci. USA* **115**, 4206–4211. (doi:10.1073/pnas.1802811115)
53. Murtada S-I *et al.* 2020 Data from: Paradoxical aortic stiffening and subsequent cardiac dysfunction in Hutchinson–Gilford progeria syndrome. Dryad Digital Repository. (https://dx.doi.org/10.5061/dryad.mcvdncjw9)